

# Identification of tidal features in deep optical galaxy images with Convolutional Neural Networks

H. Domínguez Sánchez<sup>1,2\*</sup>, G. Martín<sup>3,4</sup>, I. Damjanov<sup>5</sup>, F. Buitrago<sup>6,7</sup>, M. Huertas-Company<sup>8,9,10</sup>, C. Bottrell<sup>11</sup>, M. Bernardi<sup>12</sup>, J. H. Knapen<sup>8,9</sup>, J. Vega-Ferrero<sup>6,8,9</sup>, R. Hausen<sup>13</sup>, E. Kado-Fong<sup>14</sup>, D. Población-Criado<sup>15</sup>, H. Souchereau<sup>5,16</sup>, O. K. Leste<sup>17</sup>, B. Robertson<sup>18</sup>, B. Sahelices<sup>15</sup>, K.V. Johnston<sup>19</sup>

<sup>1</sup> Centro de Estudios de Física del Cosmos de Aragón (CEFCA), Plaza San Juan, 1, 44001, Teruel, Spain

<sup>2</sup> Institute of Space Sciences (ICE, CSIC), Campus UAB, Carrer de Can Magrans, s/n, 08193 Barcelona, Spain

<sup>3</sup> Korea Astronomy and Space Science Institute, 776 Daedeokdae-ro, Yuseong-gu, Daejeon 34055, Korea

<sup>4</sup> Steward Observatory, University of Arizona, 933 N. Cherry Ave, Tucson, AZ 85719, USA

<sup>5</sup> Department of Astronomy and Physics, Saint Mary's University, 923 Robie Street, Halifax, NS B3H 3C3, Canada

<sup>6</sup> Departamento de Física Teórica, Atómica y Óptica, Universidad de Valladolid, 47011 Valladolid, Spain

<sup>7</sup> Instituto de Astrofísica e Ciências do Espaço, Universidade de Lisboa, OAL, Tapada da Ajuda, PT1349-018 Lisbon, Portugal

<sup>8</sup> Instituto de Astrofísica de Canarias (IAC), La Laguna, 38205, Spain

<sup>9</sup> Departamento de Física - Universidad de La Laguna, La Laguna, 38205, Spain

<sup>10</sup> LERMA - Observatoire de Paris, PSL, Université Paris-Cité, Paris, France

<sup>11</sup> Kavli Institute for the Physics and Mathematics of the Universe (WPI), UTIAS, University of Tokyo, Kashiwa, Chiba 277-8583, Japan

<sup>12</sup> Department of Physics and Astronomy, University of Pennsylvania, Philadelphia, PA 19104, USA

<sup>13</sup> Department of Physics and Astronomy, The Johns Hopkins University, 3400 N. Charles St., Baltimore, MD 21218 USA

<sup>14</sup> Physics Department, Yale Center for Astronomy & Astrophysics, PO Box 208120, New Haven, CT 06520, USA

<sup>15</sup> GCME Research Group, Departamento de Informática, Universidad de Valladolid, 47011 Valladolid, Spain

<sup>16</sup> Department of Astronomy, Yale University, New Haven, CT 06511, USA

<sup>17</sup> Department of Physics and Astronomy, University of Victoria, 3800 Finnerty Rd, Victoria, BC V8P 5C2, Canada

<sup>18</sup> Department of Astronomy and Astrophysics, University of California, Santa Cruz, 1156 High Street, Santa Cruz, CA 95064 USA

<sup>19</sup> Department of Astronomy, Columbia University, New York, NY, USA

8 March 2023

## ABSTRACT

Interactions between galaxies leave distinguishable imprints in the form of tidal features which hold important clues about their mass assembly. Unfortunately, these structures are difficult to detect because they are low surface brightness features so deep observations are needed. Upcoming surveys promise several orders of magnitude increase in depth and sky coverage, for which automated methods for tidal feature detection will become mandatory. We test the ability of a convolutional neural network to reproduce human visual classifications for tidal detections. We use as training  $\sim 6000$  simulated images classified by professional astronomers. The mock Hyper Suprime Cam Subaru (HSC) images include variations with redshift, projection angle and surface brightness ( $\mu_{lim}=26 - 35$  mag arcsec<sup>-2</sup>). We obtain satisfactory results with accuracy, precision and recall values of Acc=0.84, P=0.72 and R=0.85 for the test sample. While the accuracy and precision values are roughly constant for all surface brightness, the recall (completeness) is significantly affected by image depth. The recovery rate shows strong dependence on the type of tidal features: we recover all the images showing *shell* features and 87% of the tidal *streams*; these fractions are below 75% for *mergers*, *tidal tails* and *bridges*. When applied to real HSC images, the performance of the model worsens significantly. We speculate that this is due to the lack of realism of the simulations and take it as a warning on applying deep learning models to different data domains without prior testing on the actual data.

**Key words:** galaxies: structure – methods: observational – surveys

## 1 INTRODUCTION

In the standard  $\Lambda$ -Cold Dark Matter ( $\Lambda$ CDM) cosmology scenario, small scale overdense perturbations in the early Universe collapse

\* Corresponding author: hdominguez@cefca.es

first and produce dark matter haloes that accumulate baryons at the centre. The small structures aggregate successively into larger structures via mergers in a process known as hierarchical growth (White & Rees 1978; Fall & Efstathiou 1980; White & Frenk 1991; Lacey & Cole 1993). In addition, accretion processes of small satellite galaxies or gas in filaments produce a vast and complex network of ultra-low surface brightness streams which should be present around all galaxies (e.g., Pillepich et al. 2014 and references therein).

Therefore, galaxy mergers have a fundamental and critical role within the  $\Lambda$ CDM cosmogony. While there is a general consensus that the merger fraction increases with galaxy stellar mass, both from simulations (e.g., Rodríguez-Gomez et al. 2016; Huško et al. 2022) and observations (van Dokkum et al. 2010; López-Sanjuan et al. 2012; Rodríguez-Puebla et al. 2017), the relative contribution of in-situ star formation and accreted stellar mass remains an open question across much of the galaxy mass spectrum (e.g., Qu et al. 2017; Fitts et al. 2018; Conselice et al. 2022). The rate of major and minor merger events, and their impact on galaxy mass assembly and morphological transformations, are also under debate (e.g. Lotz et al. 2011; Lofthouse et al. 2017; Martin et al. 2017, 2018, 2021).

Minor mergers (with baryonic mass ratios below 1:4) are expected to be significantly more common than major ones (e.g., Cole et al. 2000; Lotz et al. 2011), and to remain frequent even at the present epoch (although this is still under debate, see for example O’Leary et al. 2021). As minor mergers do not necessarily destroy pre-existing stellar disks (e.g., Robertson et al. 2006), signs of recent or ongoing minor mergers should be apparent around galaxies in the form of stellar tidal features, which extend into the halo of the central galaxy. Merger remnants which are only a few dynamical periods old should leave distinguishable imprints in the outskirts of galaxies. The frequency and characteristics of these features hold vital clues to the nature of the events which have created them (Hernquist & Quinn 1989; Mihos et al. 1998; Helmi & White 1999; Martínez-Delgado et al. 2009; Hendel & Johnston 2015; Spavone et al. 2020; Montes et al. 2020; Vera-Casanova et al. 2022) and can thus be used to disentangle the different formation channels. Following Duc et al. (2015), *tails* are expected to be pulled out material from a gas-rich disc galaxy, while *streams* would be stripped material from a low-mass companion being consumed by the primary galaxy. Other features such as *fans* and *plumes* are expected to come from dry, major mergers. In addition, *clouds* and *shells* are expected to be the result of interactions with radial orbits, while *great circles* are more predominant for circular orbits events (Johnston et al. 2008).

Unfortunately, the majority of tidal features have very low surface brightness, expected to be fainter than  $29 \text{ mag arcsec}^{-2}$  in the  $r$ -band (Bullock & Johnston 2005; Cooper et al. 2013), and extremely deep observations are necessary to detect them, as shown explicitly in Conselice et al. (2000); Ji et al. (2014); Bottrell et al. (2019a); Thorp et al. (2021) and Mancillas et al. (2019), where the authors find two and three times more streams based on a surface brightness cut of  $33 \text{ mag arcsec}^{-2}$  than with  $29 \text{ mag arcsec}^{-2}$ . Although there is an increasing interest in the literature on the identification and characterization of tidal features, most works focus on the detailed analysis of a small number of objects via visual inspection (e.g., Martínez-Delgado et al. 2010; Javanmardi et al. 2016; Morales et al. 2018; Martínez-Delgado et al. 2021; Valenzuela & Remus 2022; Huang & Fan 2022; Sola et al. 2022), some of them belonging to local groups or clusters of galaxies (e.g., Iodice et al. 2017; Mihos et al. 2017; Spavone et al. 2018). A sample of 92 ETGs galaxies from ATLAS<sup>3D</sup> was presented in Duc et al. (2015), reporting signs of interactions or perturbed morphologies in more

than half of them, thanks to an observing strategy and data reduction pipeline optimized for low surface brightness features. Hood et al. (2018) present a visual identification of galaxies with tidal features based on DECam Legacy Survey images ( $r$ -band  $3\sigma$  depth of  $\sim 27.9 \text{ mag arcsec}^{-2}$ ) but due to the small area inspected ( $100 \text{ arcsec}^2$ ), less than 200 of them have tidal features detected with high confidence. One of the largest catalogues of tidal detections up to date was presented in Kado-Fong et al. (2018) using The Hyper Suprime-Cam Subaru Strategic Program (HSC-SSP, Miyazaki et al. 2012) data. The authors applied a filtering algorithm that iteratively separates low and high spatial frequency features of images, resulting in a sample of  $\sim 1200$  galaxies with tidal detections from a sample of  $\sim 20,000$ .

With the arrival of large imaging surveys such as Euclid (Lau-reijs et al. 2011) and the Vera Rubin Observatory’s Legacy Survey of Space and Time (LSST, Ivezić et al. 2019), the detection of these features via visual inspection is unfeasible and automated methods become imperative. The use of supervised deep learning for the analysis of galaxy images, such as convolutional neural networks (CNN), has proven to be extremely successful for classifying galaxy images (e.g. Dieleman et al. 2015; Huertas-Company et al. 2015; Domínguez Sánchez et al. 2022; Cheng et al. 2020; Vega-Ferrero et al. 2021; Walmsley et al. 2022; Hausen & Robertson 2020; Ghosh et al. 2020), including classifications of relatively rare objects such as strong lensed galaxies (Lanusse et al. 2018; Cheng et al. 2020) or post-mergers (e.g., Bickley et al. 2021). However, one of the main drawbacks of supervised learning approaches is the need for a large sample of labelled galaxies (of the order of thousands) to train and test the algorithm and its performance in different regimes (see Huertas-Company & Lanusse 2022 for a review on the topic). An alternative is the use of simulations: the viability of using galaxies from hydrodynamical simulations to train deep learning models to classify real galaxies and mergers has indeed been shown in Bottrell et al. (2019b) and Huertas-Company et al. (2019). The scarcity of a large number of galaxies showing tidal features to be used as training data has prevented to develop automated supervised detection algorithms and so far there have been almost no attempts in the literature to this respect. A pioneering effort to develop a CNN for tidal stream detection was presented in Walmsley et al. (2019), where the authors used imaging for the Canada–France–Hawaii Telescope Legacy Survey-Wide Survey (Gwyn 2012). However, the models only achieved a 76 percent accuracy, probably due to the small size of the training sample ( $\sim 1700$  galaxies, of which only 305 showed tidal stream detections).

In this work, we use synthetic HSC images of galaxies generated by the NEWHORIZON cosmological simulations (Dubois et al. 2021) to examine the viability of using CNNs to identify galaxies with tidal features. The original sample, described in Section 2, includes  $\sim 6000$  images at different surface brightness limits classified by professional astronomers. This is the largest catalogue of tidal features based on visual classification up to date. We describe our CNN and training strategy in Section 3 and test the ability of the CNNs to recover human-like classifications in Section 4, where we present the performance of the model as a function of the feature class (Section 4.1), redshift (Section 4.2) and image depth (Section 4.3). The outcome of applying the models to real data are discussed in Section 5, including an attempt of using the Kado-Fong et al. (2018) classification as a training sample. We summarise our results and discuss their implications in Section 6.

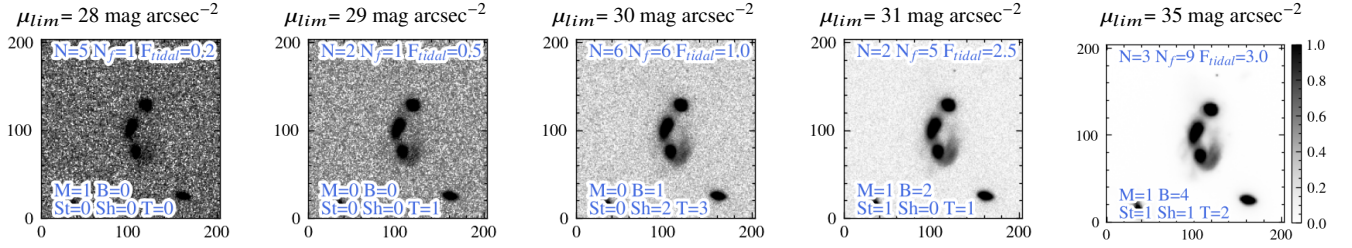


**Figure 1.** Example of the classification performed in M22. Images of the same galaxy observed at  $z=0.05$  with different  $\mu_{lim}$  (28, 29, 30, 31, 35 mag arcsec $^{-2}$ , from left to right) were classified by a varying number of astronomers ( $N$ ) into different categories. The number of observed features of each class is reported in the cutouts ( $St$ =streams,  $Sh$ =shells,  $T$ =tails,  $M$ =mergers,  $B$ =bridges) along with the total number of features ( $N_f$ ) and  $F_{tidal}=N_f/N$ . In this work we consider as positive examples those images with  $F_{tidal} > 1$ , negative those with  $F_{tidal}=0$  and uncertain otherwise. Following this criteria, the images with  $\mu_{lim}=28$  and 29 have an uncertain classification, while those with  $\mu_{lim} > 29$  are classified as showing tidal features. The cutouts are normalized in the (0,1) range using *arcsinh stretch*, as described in Section 3.1.

## 2 DATA

We take advantage of the galaxy images and labelling presented in Martin et al. (2022, hereafter M22). The galaxies are generated with NEWHORIZON, state-of-the-art cosmological hydrodynamical simulations (Dubois et al. 2021), a zoom-in of the parent HORIZON-AGN simulation (Dubois et al. 2014). NEWHORIZON combines high stellar mass ( $1.3 \times 10^4 M_\odot$ ) and spatial resolution ( $\sim 34$  pc) with a contiguous volume of (16 Mpc) $^3$ . Given the diffuse nature of galaxy stellar haloes, the trade off between resolution and volume is an important consideration. The simulations adopt the cosmological parameters from Komatsu et al. (2011,  $\Omega_m = 0.272$ ,  $\Omega_\Lambda = 0.728$ ,  $\Omega_b = 0.045$ ,  $H_0 = 70.4$  km s $^{-1}$  Mpc $^{-1}$ ). We refer the reader to M22 for more technical details on the simulations.

### 2.1 Mock galaxy images

The parent sample consists of 36 unique galaxies, with masses above  $10^{9.5} M_\odot$  at  $z=0.2$ , and their progenitors at  $z=0.4$ , 0.6 and 0.8. Realistic HSC-like mock images are generated by convolving the smoothed star-particle fluxes with the  $g$ -band HSC 1D PSF (Montes et al. 2021). Three projections of each snapshot ( $xy$ ,  $xz$ ,  $yz$ ) are created at 5 different distances (corresponding at  $z=0.05$ , 0.1, 0.2, 0.4 and 0.8). The physical field of view is 100 kpc (proper) cropped from the initial 1 Mpc cube. Mock images are produced for each galaxy by extracting star particles centred around each galaxy. The spectral energy distribution (SED) for each star particle is then calculated from a grid of Bruzual & Charlot (2003) simple stellar population models assuming a Salpeter (1955) IMF. They account for dust attenuation of the SEDs using a screen model in front of each particle for which a gas-to-dust ratio of 0.4 Draine et al. (2007) and a Weingartner & Draine (2001)  $R = 3.1$  Milky Way dust grain model are assumed. After redshifting each particle SED, the flux of each particle is calculated by convolving with the appropriate bandpass transmission function. Finally, random Gaussian noise is added to the simulated images to reach different limiting surface brightness  $\mu_r^{lim}$  corresponding to 28, 29, 30, 31 and 35 mag arcsec $^{-2}$  ( $3\sigma$ ,  $10'' \times 10''$ ). The combination of these parameters results in 10800 unique simulated images. Since the pixel angular size is fixed, the difference in distance of the galaxies directly translates into cutouts of different sizes (26 $\times$ 26, 36 $\times$ 36, 60 $\times$ 60, 108 $\times$ 108, 204 $\times$ 204 pixels, from  $z=0.8$  to  $z=0.05$ ). In order to increase the sample size and to have mock images which resemble current observations better, we have generated 2 $\times$ 1453 additional snapshots with  $\mu_{lim}=26$  and 27 mag arcsec $^{-2}$  by adding Gaussian noise following Equation 3 from

M22 to the deepest available image of each particular counterpart (i.e., with the corresponding ID, snapshot, redshift and projection).

### 2.2 Tidal feature classification

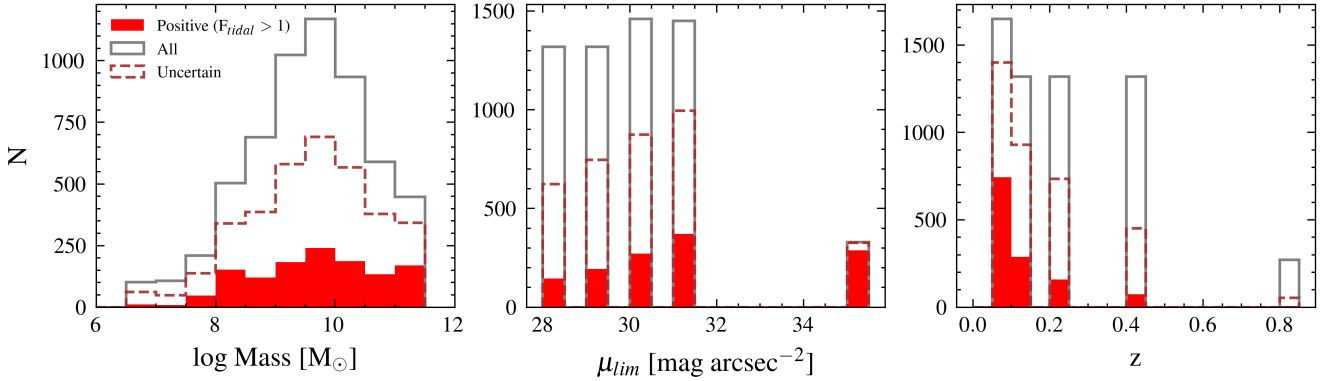
M22 performed a visual inspection of  $\sim 8000$ <sup>1</sup> unique images by 45 expert classifiers, with a random subset of them classified six times, by identifying the presence of tidal features and classifying them into stellar *streams*, *tidal tails*, *shells*, *tidal bridges*, *merger remnants*, *double nuclei* or *miscelanea*.<sup>2</sup> The classification was summarized in a catalogue including 5 835 unique images. The missing images were not included in the classification catalogue for being too noisy. We use this catalogue as parent sample in our work. The visually classified images were created at HSC pixel angular scale of 0.2'', but rescaled to 1'', comparable to the FWHM of the PSF used (an observer might reasonably rebin like this in order to gain additional depth without losing any detail). This rebinning will have a significant impact when applying the models trained with these images to real HSC-SSP data, as we discuss in Section 5. In this work, we use the exact same images as those visually classified to train the deep learning algorithm, so that the labels are consistent.

Figure 1 shows the result of the classification for a particular galaxy image observed at redshift  $z=0.05$  with different limiting surface brightness. Each image is classified by a number of astronomers ( $N$ ) which assign the number of observed features ( $N_f$ ) of each class to the image. This means that more than one class can be assigned to each image and that the classification can change with  $\mu_{lim}$ , but also due to projection effects or spatial resolution (redshift). For this particular example, the deepest image ( $\mu_{lim}=35$  mag arcsec $^{-2}$ ) was classified by  $N=3$  astronomers which annotated features of *streams*, *shells*, *tidal tails*, *merger* and *bridges* adding up to a total of  $N_f=9$ . On the other hand, the shallower image ( $\mu_{lim}=28$  mag arcsec $^{-2}$ ) was classified by  $N=5$  astronomers, of whom only one annotated the feature class of *merger* ( $N_f=1$ ).

To the best of our knowledge, this is the sample with the largest number of tidal detections visually classified by professional astronomers up to date, making it the optimal sample for training a deep learning algorithm for automated detection of tidal features.

<sup>1</sup> Note that this number is smaller than 10 800 quoted on Section 2.1 due to missing progenitors at some snapshots which are too small to be detected by the structure finder at higher redshift.

<sup>2</sup> The *plume* and *asymmetric* categories described in M22 are combined into a single *miscelanea* category in the catalogue, since there was a large degree of overlap between the two.



**Figure 2.** Distribution of stellar mass (left), limiting surface brightness (middle) and redshift (right) of the images from the parent sample presented in M22. The grey empty histograms represent the full sample (5835 images), the red filled histograms show the images labelled as positive examples of tidal features (i.e., with  $F_{\text{Tidal}} > 1$ ), and the brown empty histograms correspond to images with uncertain classifications ( $0 < F_{\text{Tidal}} < 1$  or labelled as *misc/double nucleus* only). Note the large dependence of the fraction of tidal feature identification by the astronomers with surface brightness limit and redshift (or, equivalently, cutout size).

However, the example from Figure 1 illustrates the challenges of the visual identification of tidal features: the definition of the different classes of features is not objective and there is discrepancy between the classifiers. In some cases, the same images are classified as showing tidal features by some classifiers and as featureless by others. This is a warning about the reliability of the visual classifications and how much they should be trusted as the ground truth. Although we are well aware of these caveats, we continue to use this dataset in our analysis as is the largest and most complete galaxy sample with tidal feature labels up to date.

To simplify the problem, in this work we focus on the identification of the presence (or not) of a tidal feature, regardless of its category and, thus, we consider all the tidal feature classes simultaneously. Since the images were classified by a varying number of experts, ranging from one to six, and more than one tidal feature category could be assigned to each image, we divide the number of tidal feature identifications by the number of classifiers. We refer to this quantity as the *fraction of tidal detections*,  $F_{\text{Tidal}} = N_f / N$ , and consider certain classifications those with  $F_{\text{Tidal}} = 0$  or  $F_{\text{Tidal}} \geq 1$  (corresponding to 39% and 38% of the sample, respectively). For the images with  $0 < F_{\text{Tidal}} < 1$  (the remaining 22%) the classification of different experts were inconsistent and we refer to these cases as uncertain classifications. To avoid including uncertain classifications in the loop, we remove the images with  $0 < F_{\text{Tidal}} < 1$  from the train and test samples. After visual inspection of some images, we found that the classes *misc* and *double nucleus* do not fit exactly into the tidal features we are aiming to detect. Therefore, images classified *only* as *misc* or *double nucleus* are also removed from the analysis.

The distribution in mass, surface brightness limit and redshift of the parent sample and the images classified as showing tidal features are shown in Figure 2. The detection of tidal features by humans is largely dependent on the depth of the images and on the image size (or redshift of the galaxy), as reported by M22 and clearly seen in Figure 2. This has important consequences for the performance of the algorithm for automated detection of tidal features, as we discuss in Section 4.

### 3 METHODOLOGY

We use supervised learning for the identification of galaxies showing tidal features; i.e., we need to provide the algorithm with the ground truth we would like to recover in the form of labels (in this case, tidal feature detection or not). We use CNNs, a class of artificial neural networks consisting of convolution kernels that slide along input features and provide feature maps. These maps are then passed through a fully connected network that outputs a value, corresponding to a particular property that we want to learn. The final function (or weights of the model) is the one that minimizes the difference between the output and the input labels. In this work, the input to the CNN are single-band images in the HSC *r*-band (we use the *r*-band images since these were the images classified by the professional astronomers in M22) with their corresponding labels (0s for non-tidal detections and 1s for tidal features). The output of the model,  $P_{\text{Tidal}}$ , is the probability that the image shows a tidal feature.

#### 3.1 Image pre-processing

Before being fed to the CNN, the galaxy images are normalized in the range (0,1) to avoid operating with very large numbers. For the normalization, the commonly used *asinh stretch* function<sup>3</sup> (see Lupton et al. 2004) is used, combined with a sigma clipping of 3% of the faintest and the brightest pixels of each image. This pre-processing enhances the detection of low surface brightness features. The images are converted to the same size,  $69 \times 69$ , (the input to the CNN is an array of fixed dimensions) by rebinning or interpolating the pixel flux, depending on the original image size. We tested input sizes of  $100 \times 100$  without obtaining significant changes in the results. Throughout the paper we use the  $69 \times 69$  stamps as reference.

#### 3.2 Input Labels

We use a binary classification to separate images which show tidal features (positive samples, labelled as 1s) from images without tidal signatures (negatives, labelled as 0s). Therefore, we unify all classes

<sup>3</sup> <https://docs.astropy.org/en/stable/api/astropy.visualization.AsinhStretch.html>



Layer Type	Output shape	Parameters
Input	(69, 69, 1)	0
Conv2D	(69, 69, 32)	320
MaxPooling2D	(34, 34, 32)	0
Conv2D	(34, 34, 48)	13 872
MaxPooling2D	(17, 17, 48)	0
Conv2D	(17, 17, 64)	12 352
MaxPooling2D	( 8, 8, 64)	0
Flatten	(4096)	0
Dense	(64)	262 208
Dense	(1)	65
Total number of parameters		288 817

**Table 1.** Architecture of the CNN used in the main text.

of tidal features into a single one (detections or non-detections). As explained in Section 2.2, we use the quantity  $F_{\text{Tidal}}$  to select positive and negative examples, and leave out of the analysis images with uncertain classifications.

For the images generated specifically for this work at  $\mu_{lim}=26$ , 27 mag arcsec<sup>-2</sup>, we do not have classifications by the professional astronomers as these images were not part of the original M22 sample. We choose to use the labels of their counterpart images (i.e., with the same galaxy ID, snapshot, redshift and projection) at  $\mu_{lim}=28$  mag arcsec<sup>-2</sup> as their ‘ground truth’ label. This exercise allows us to test whether or not the algorithm can recover visually classified features in images with surface brightness limit 2 mag arcsec<sup>-2</sup> shallower than the images used for their visual classification.

We randomly split the sample in 85% for training (resulting in 4418 images, out of which 1539 are tidal detections) and reserve 15% for testing (820, out of which 223 are tidals).

### 3.3 CNN architecture

The CNN architecture discussed in the main text, based on the one presented in Walmsley et al. (2019), is summarized in Table 1. It consists on three 2D convolution layers with 32, 48 and 64 filters with sizes 3, 3, and 2, respectively and 2×2 *max-pooling* windows. They are followed by a fully connected layer with 64 neurons, Rectified Linear Unit (ReLU) non-linear activation function and 0.5 dropout rate. A final single neuron outputs values converted to the (0,1) range by applying a sigmoid function. Binary-crossentropy is used as loss function and Adam as optimizer. The number of free parameters of this CNN is 288 817 (for input sizes 69×69×1).

We have tested other CNN architectures, namely the one commonly used by the authors (e.g., Domínguez Sánchez et al. 2018 and Domínguez Sánchez et al. 2022), consisting on four 2D convolutional layers with 32, 64, 128 and 128 filters with sizes 6, 5, 2 and 3, 2×2 *max-pooling* and 0.25 dropout<sup>4</sup>, followed by a fully connected layer with 64 neurons and 0.25 dropout. The number of free parameters is 2 600 545, almost ten times larger than in the Walmsley et al. (2019) CNN. A variation of the Domínguez Sánchez et al.

(2018) architecture, with filter sizes (3, 3, 2, 3) and adding a fully connected layer with 16 neurons before the final layer, has also been tested. In addition, conventional networks such as ResNet-18,-50,-101 (He et al. 2016) and EfficientNet-B0,-B1, -B4 and -B7 (Tan & Le 2019) have been attempted. As the use of more complicated CNNs did not significantly improve the results, we have decided to use the Walmsley et al. (2019) architecture as a reference due to its simplicity with respect to other algorithms.

We use an overall standard strategy for training. We train for 100 epochs with a batch size of 100 and a validation split of 0.2 (from the training sample). Data augmentations are performed while training, including vertical and horizontal flip, weight and height shifts (by 0.05%), zoom in and out (0.75-1.3) and rotations (0, 90, 180, 270 degrees). We train 10 independent models, randomly changing the initialization weights and the training and validation sets. During the training we observed no signs of over-fitting. The results presented in the following sections are based on the average of the output of the 10 models, which we refer to as  $P_{\text{Tidal}}$ .

## 4 RESULTS

In this section, we study the performance of our models when applied to the test dataset. We consider two different tests sets: the one containing only the original simulations and labels by professional astronomers (i.e., surface brightness  $\mu_{lim} \geq 28$  mag arcsec<sup>-2</sup>) and the test set which includes the original and the simulated images at  $\mu_{lim}=26, 27$  mag arcsec<sup>-2</sup>. We will refer to the former as the *original* test sample and to the latter as the *original+shallow* test sample.

We use standard metrics for studying the performance of the models:

$$\text{Accuracy} = \frac{\text{TP} + \text{TN}}{\text{TP} + \text{TN} + \text{FP} + \text{FN}} = \frac{\text{TP} + \text{TN}}{\text{Total}} \quad (1)$$

$$\text{Precision} = \frac{\text{TP}}{(\text{TP} + \text{FP})} = \frac{\text{TP}}{P_{\text{pred}}} \quad (2)$$

$$\text{Recall} = \frac{\text{TP}}{(\text{TP} + \text{FN})} = \frac{\text{TP}}{P_{\text{input}}} \quad (3)$$

$$\text{F1} = 2 \times \frac{P \times R}{(P + R)} \quad (4)$$

where TP, TN, FP and FN stand for true positives, true negatives, false positive and false negative, respectively, while  $P_{\text{pred}}$  and  $P_{\text{input}}$  are the total number of predicted and input positives, respectively. To separate the instances into positive and negative predictions, we use the *binary classification threshold probability*,  $P_{\text{th}}$ , which is the value that optimizes the true positive rate (TPR, i.e. the fraction of correctly identified tidal detections) and the false positive rate (FPR, i.e., the fraction of non tidals classified as tidal detections) simultaneously. The number of galaxies in each test sample and the fraction of positives (labelled as tidal detections in the input catalog), as well as the accuracy, precision, recall and F1 score of each sample is reported in Table 2. The accuracy is the fraction of correctly classified instances, the precision is the fraction of TP among the instances classified as positive (analogue to the purity), while the recall is the fraction of TP among the positive

<sup>4</sup> This is a slight modification with respect to the original configuration.

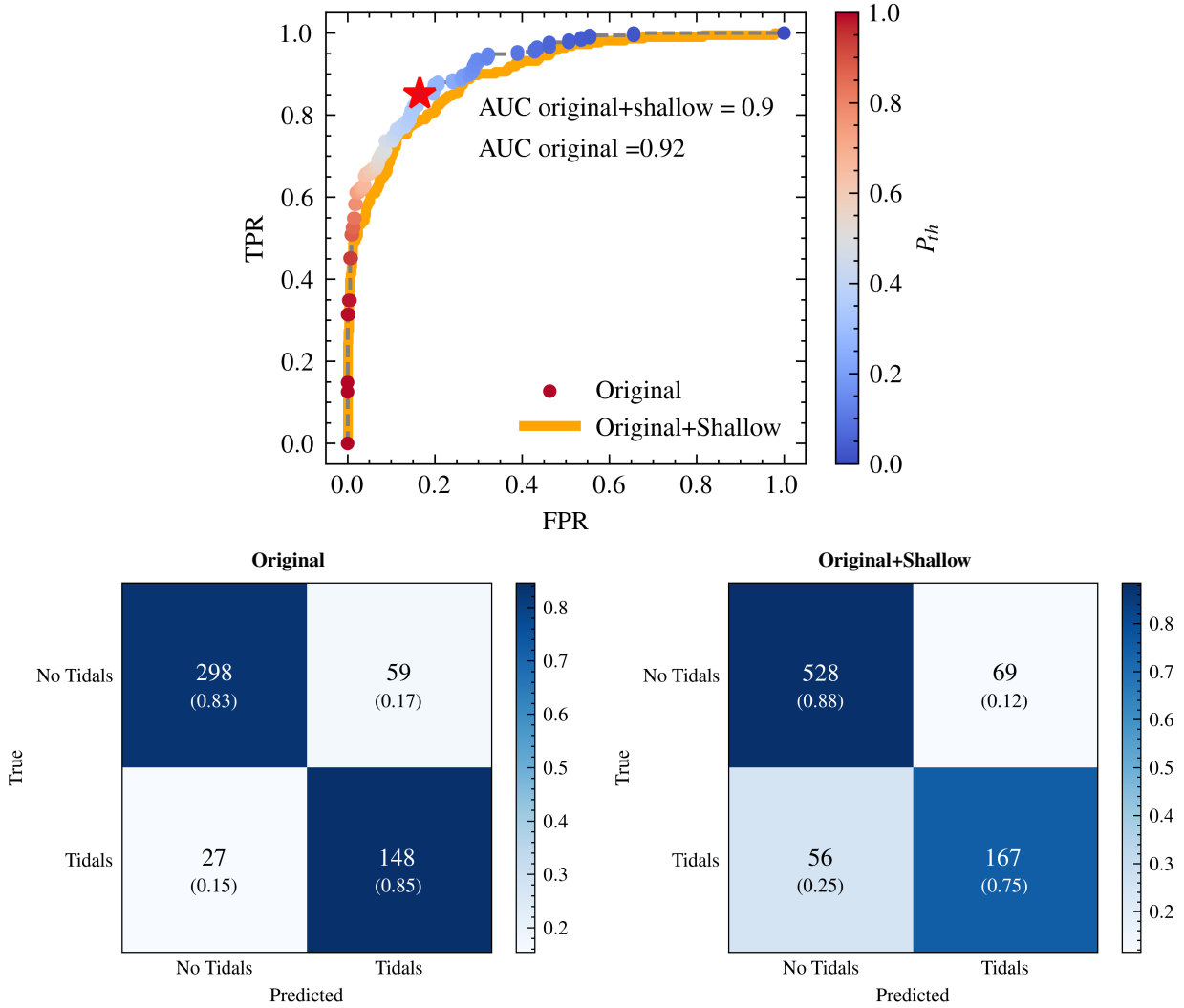


**Figure 3.** *Upper panel:* ROC curve - True Positive Rate as a function of False Positive Rate - for the *original* (circles, colored coded by  $P_{th}$ ) and *original+shallow* (orange line) test samples. The red star marks the optimal threshold for the *original* sample. *Bottom panels:* Confusion Matrix for the *original* (left) and *original+shallow* test sample (right) obtained when selecting positive samples as those above the corresponding  $P_{th}$  of each sample. Input labels are shown in the y-axis, predictions in the x-axis. The number of objects is reported in each quadrant, color coded by the fraction of that particular true class (also shown in parenthesis).

Test sample	$N_{test}$	% Positives	$P_{th}$	Accuracy	Precision	Recall	F1
Original	532	33	0.32	0.84	0.72	0.85	0.78
Original+shallow	820	27	0.31	0.85	0.71	0.75	0.73

**Table 2.** Number of galaxies in the *original* and *original+shallow* test samples, and the fraction of those labelled as tidal features, as well as the accuracy, precision, recall and F1 score obtained when selecting as positive predictions the images with model scores above their corresponding  $P_{th}$ .

input instances (analogue to the completeness). Finally, the F1 score is the harmonic mean of the two.

Figure 3 shows the receiver operating characteristic curve (ROC) that represents TPR versus FPR as the discrimination threshold ( $P_{th}$ ) is varied. An adequate classifier would maximize the TPR while keeping the FPR low. The area under the ROC curve (AUC) is above 0.9 in both cases (a perfect classifier would have AUC=1). We also show the confusion matrices for the two test samples using as probability threshold the optimal value for each sample to separate the predictions into positive and negative classes. As re-

ported in table 2, the accuracy (Equation 1) for the *original* and *original+shallow* test samples is 0.84 and 0.85, while the precision (or purity, Equation 2) is 0.72 and 0.71, respectively. These values are surprisingly similar, taking into account the inclusion of  $\sim 300$  images with  $\mu_{lim} < 28$  in the *original+shallow* test sample for which the ground truth is assumed to be the labels at  $\mu_{lim} = 28$ , i.e., those reported for images two magnitude deeper than the actually classified images. The main difference is in the recall (or completeness, Equation 3), that drops from 0.85 for the *original* test sample to and 0.75 for the *original+shallow* test sample.

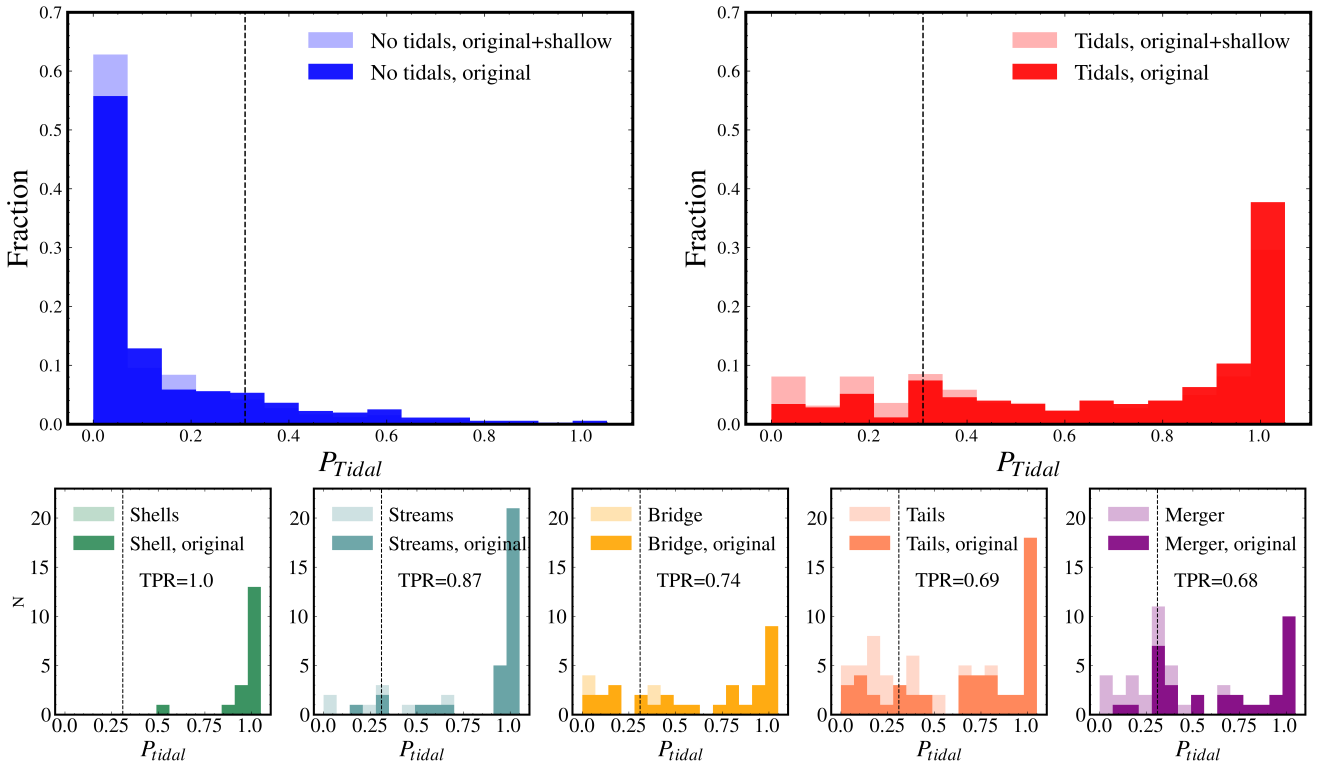


**Figure 4.** *Upper panels:* Output probability distribution of the model for tidal detection,  $P_{Tidal}$ , for the test sample divided into non-tidal visual classifications (left panel, blue) and tidal visual classifications (right panel, red). Darker colors represent the *original* sample, lighter colors the *shallow* sample. *Lower panels:*  $P_{Tidal}$ , for the test sample divided into different categories, as stated in the legend. The dashed line is  $P_{th} = 0.31$ , the threshold used to define an instance as positive or negative. The true positive rate (TPR) of each category for the *original+shallow* sample is reported in the corresponding panel.

As expected, it is more difficult for the algorithm to recover tidal detections in shallower images. We discuss the surface brightness dependence of the classification in Section 4.3. Since the precision values are very similar for the two test samples but recall is smaller for the *original+shallow* test sample, the F1 score (Equation 4) is also lower for the *original+shallow* (F1=0.73) than for the *original* sample (F1=0.78).

#### 4.1 Dependence on tidal feature class

Now we study the ability of our CNN to detect different classes of tidal features. Figure 4 shows the output probability of our model,  $P_{tidal}$  (larger values correspond to more confident detection of tidal features), divided in the classes provided in the M22 catalogue. Clearly, there are classes which are easier to identify than others. For example, all the *shells* in the test sample are recovered, and the TPR for the *streams* is 0.84, while for *mergers* or *tidal tails* is below 0.7. It is also evident from Figure 4 that the model performs worse for the *shallow* sample: the  $P_{tidal}$  values are lower for the positive cases of this sub-sample. We discuss in more detail the effect of the  $\mu_{lim}$  in section 4.3.

Figure 5 shows representative examples of TP identifications of *shells*, *streams* and *mergers* at different surface brightness limits. The features are very evident for the deep images (right panels) and, in some cases, it is surprising that the model is able to identify the tidal features in the more noisy images (left panels). Besides, the cutouts are displayed at their original size, not binned to  $69 \times 69$ , which is the input to the CNN. These examples show that *shells* and *streams* are easier to identify by eye than *mergers*. We note, however,

that the number of *shells* in the test sample is small (12) and that there are no *shells* in the *shallow* test sample. This is due to the fact that there are no visually identified *shells* in images shallower than  $\mu_{lim}=28$  mag arcsec $^{-2}$ , from which the labels for the *shallow* sample come from. In other words, the fact that we are recovering more *shells* may be due to these structures being identified by eye only in the deeper images. We note again that the different classes reported in the M22 catalogue are not mutually exclusive (see also Figure 1), and therefore images identified as *shells* can also fall into other categories (this happens indeed for 10 out of 12 *shells* in the test sample).

FN cases are shown in Figure 6 for *streams* and *mergers*. As all the *shells* in the test sample are correctly identified by our model, there are no FN for this category. Even for the deeper images (right panels) it is difficult to identify the tidal features, while the shallower images (left panels) are dominated by noise. Therefore, it is not surprising that the model fails in these cases.

#### 4.2 Dependence with redshift

In this section, we report the performance of the model when the test sample is divided into different redshift bins, which is directly related to the original stamp size (the stamps are then resampled into  $69 \times 69$  because the input to the CNN has fixed dimensions, see details in Section 2 and 3.1). Figure 7 shows the ROC curves as a function of redshift. As expected, the larger AUC is obtained in the lower redshift bin ( $z=0.05$ ). However, the dependence on redshift is not very strong and not even linear. For example, the AUC is larger for  $z=0.4$  (AUC=0.81) than for  $z=0.2$  (AUC=0.76), probably due

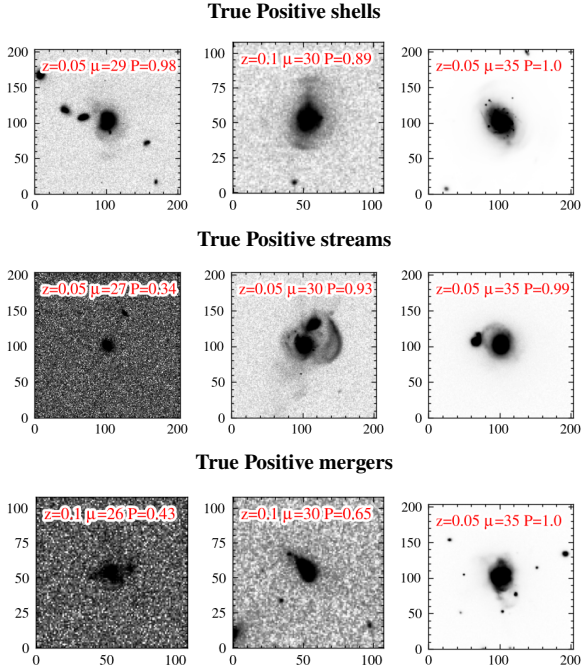


**Figure 5.** TP examples of shells, streams and mergers, from top to bottom. The cutouts have been processed as described in Section 3.1, but are shown at their original sizes (i.e., they are not binned to  $69 \times 69$ , which is the input to the CNN), and the  $x$  and  $y$  axes correspond to the number of pixels. The information shown in each cutout corresponds to the redshift, the surface brightness limit (increasing from left to right) and the output probability of the model,  $P_{\text{Tidal}}$ .

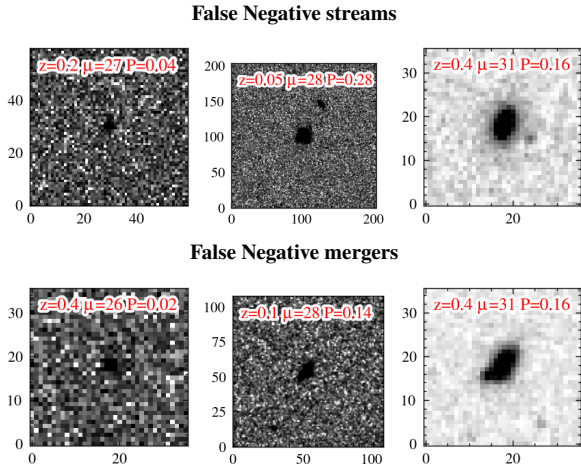


**Figure 6.** Same as figure 5 but for FN examples of *streams* and *mergers* (top and bottom panels, respectively). Note that there are no false negative shells (see Figure 4). The features are hard to detect by eye, so it is not surprising that the model fails in these cases.

to the lower fraction of visual detections at higher redshifts, which increases the overall accuracy. This is evident for  $z=0.8$  (shown as a dotted line), where there are no galaxies classified as tidal detections in the test sample, neither in the input labels nor by our model, and therefore the accuracy is 100%.

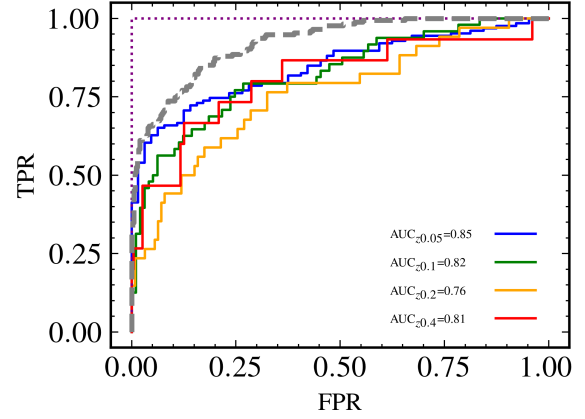


**Figure 7.** ROC curves for galaxies at different redshifts, color coded as indicated by the legend. The gray dashed line shows the ROC curve for the full *original* sample. Note that there are no positive cases at  $z=0.8$ , and the model correctly classifies all the images at this  $z$  as negatives; hence we represent the ROC curve as the dotted purple line.

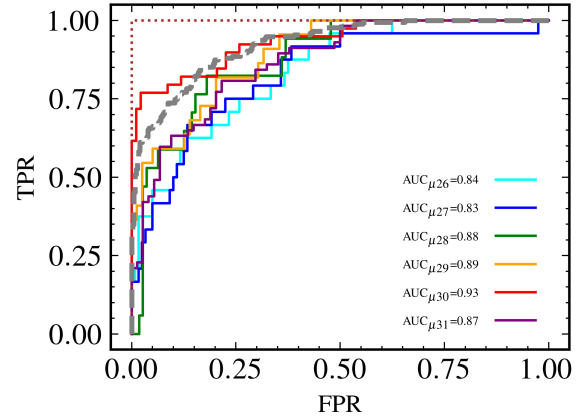


**Figure 8.** Same as figure 7 for images at different surface brightness, color coded according to the legend. Note that at  $\mu=35$  mag arcsec $^{-2}$  all images show tidal features and are correctly classified as such by our model (we plot the ROC curve as the brown dotted line)

### 4.3 Dependence with surface brightness

Finally, we study the dependence of the model performance on the surface brightness of the images to be classified. Figure 8 shows the ROC curve for the different  $\mu_{\text{lim}}$  values. The lower AUC correspond to the shallower images ( $\mu=26, 27$ ), as expected, and the best results are obtained for  $\mu=30$  mag arcsec $^{-2}$ . We show the ROC curve for  $\mu=35$  mag arcsec $^{-2}$  as dotted line because all the images from the test sample are classified as tidal detections, both in the input catalogue and by the model (just the opposite of what happens at  $z=0.8$ ). Surprisingly, the AUC at  $\mu=31$  mag arcsec $^{-2}$  is lower (AUC=0.87) than at  $\mu=30$  mag arcsec $^{-2}$  (AUC=0.93) and comparable to the values obtained at  $\mu=28$  mag arcsec $^{-2}$ .

To shed more light on the classification efficiency, Figure 9 shows the confusion matrices (generated by setting  $P_{\text{th}}=0.31$ ) for three surface brightness limits ( $\mu=26, 30, 31$  mag arcsec $^{-2}$ ). These confusion matrices highlight the fact that the large AUC for  $\mu=26$  mag arcsec $^{-2}$  is mainly driven by the ability of the classifier to correctly identify images without tidal detections (98% accuracy



for the negative subsample), while it struggles to correctly classify the tidal detections (only 33% are recovered in this surface brightness range). On the other hand, at  $\mu=31$  mag arcsec $^{-2}$  the contrary happens: the model is able to correctly identify 89% of the tidal detections, at the cost of misclassifying 35% of the non-detections. At  $\mu=30$  mag arcsec $^{-2}$  the model is able to correctly identify 90% of the tidal detections while keeping the contamination (i.e., the number of FP) at 26%.

While this trend could be expected, and is in line with the larger fraction of tidal detections obtained in deeper images by visual inspection (see Figure 2), it could be an indication that our model has, at least to some extent, learned the signal-to-noise of the images: it tends to classify deeper images more frequently as tidal detections. To test this assumption, Figure 10 shows the accuracy, precision and recall for each surface brightness bin, as well as the fraction of positive samples (tidal detections) in the input catalogue.

As reflected by the confusion matrices, the recall (completeness) of the model is highly dependent on the depth of the images to be classified, going from around  $R \sim 0.40$  at  $\mu=26$  mag arcsec $^{-2}$  to  $R \sim 0.90$  at  $\mu=31$  mag arcsec $^{-2}$ . However, this is not as clearly reflected in the precision (purity) values, roughly constant and above  $P \sim 0.60$  at all surface brightness. In the same way, the accuracy is stable throughout the whole magnitude range ( $\sim 80\%$ ), indicating that the model has not simply learned the signal-to-noise of the images. The fact that the accuracy does not improve with  $\mu_{lim}$ , even if the recall (completeness) does, can be explained by a larger fraction of FP. However, the increase in FP does not decrease the precision (purity) because of the larger fraction of tidal detections in the input catalogue at higher  $\mu_{lim}$  (black symbols in Figure 10), which together with the larger recall, increase the number of TP to counterbalance the larger number of FP.

We would like to highlight here again that the labels used for the *shallow* sample ( $\mu_{lim} < 28$  mag arcsec $^{-2}$ ) correspond to the visual classification of the images with  $\mu=28$  mag arcsec $^{-2}$ , which explains the drop in completeness in this surface brightness regime. Indeed, it is remarkable that our model is able to recover 40% of the images with tidal detections, even when the images are 2 orders of magnitude shallower than the ones used for labelling. This is in agreement with recent results suggesting that CNNs trained with ‘intrinsic’ ground truth can recover astronomical features hidden to the human eye (see e.g., Vega-Ferrero et al. 2021). This result could have a large impact on the design strategy of future surveys.

We emphasize that redshift and surface brightness limits are intertwined in the current analysis. Unfortunately, the test sample size is too small to examine the trends at each  $\mu_{lim}$  limit separately, at fixed redshift (or viceversa).

## 5 APPLICATION TO REAL HSC-SSP DATA

Our models are trained in HSC-like mock images. Therefore, it is important to test the performance of the algorithm in real data with similar characteristics to the training dataset. We thus use images from the HSC-SSP survey (Hyper Suprime-Cam Subaru Strategic Survey) Wide layer Aihara et al. 2018a,b. The HSC Wide layer covers the largest on-sky area at a relatively shallow depth ( $i \sim 26$ ) relative to the Deep and UltraDeep Layers ( $i \sim 27$  and  $i \sim 28$ , respectively).

In particular, we have applied our models to the HSC-SSP images presented in Kado-Fong et al. (2018). These are  $\sim 21,000$  galaxies from the internal data release S16A, with spectroscopic redshifts from SDSS at  $0.05 < z < 0.45$ . Kado-Fong et al. (2018) used

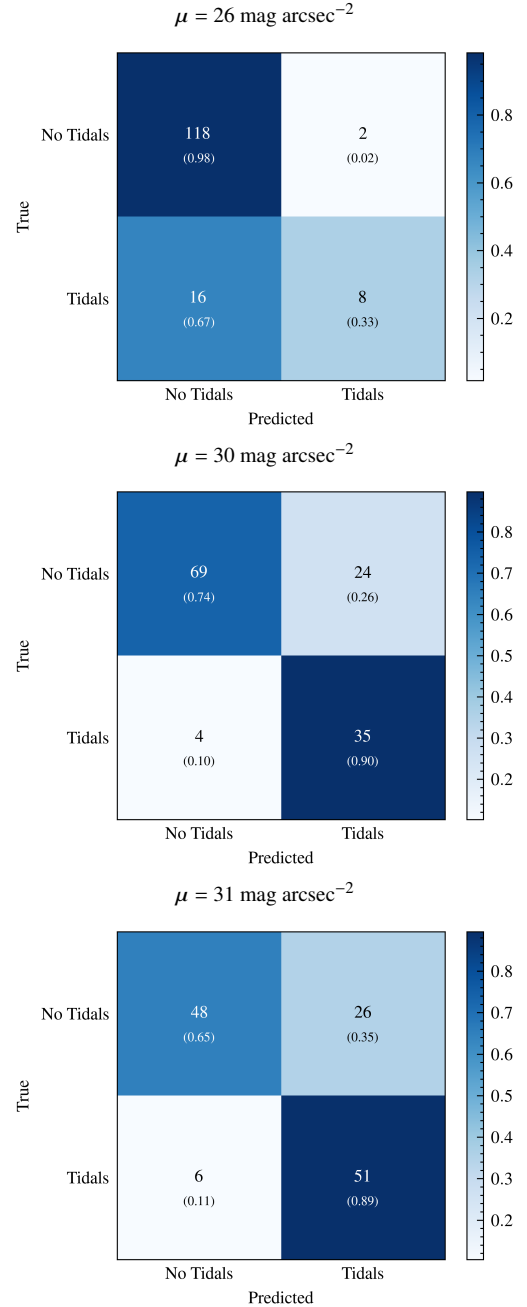


**Figure 9.** Confusion matrices for three different surface brightness bins:  $\mu_{lim}=26, 30, 31$  mag arcsec $^{-2}$ , from top to bottom. The number of objects is reported in each quadrant, color coded by the fraction of that particular true class (also shown in parenthesis).

a filtering algorithm to identify tidal features, combined with visual classification of the features detected by such filtering, resulting in a sample of  $\sim 1,200$  tidal feature detections. Our first approach to this work was to use the labels from Kado-Fong et al. (2018) sample to train the algorithm for tidal stream identification, but after exhaustive testing, the results were not good enough ( $F1=0.37$ ), mostly due to the small completeness achieved by the models ( $R=0.26$ ).

As previously explored in the context of tidal feature classification of mock images (Section 2.2), one source of significant label noise is the reliability of visual inspection itself. Visual inspection of the full sample by three professional astronomers (I.D., H.S.,

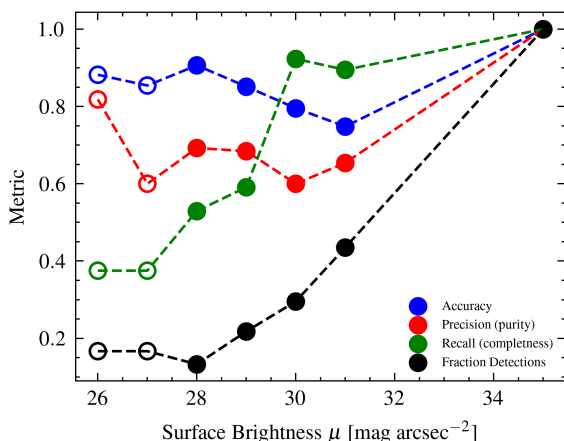


**Figure 10.** Accuracy (blue), precision (red) and recall (green) obtained for the test sample as a function of the images’ surface brightness  $\mu_{lim}$ . The fraction of tidal detections in the input catalogue is shown in black. The bins at  $\mu_{lim}=26, 27$  mag arcsec $^{-2}$  are plotted as empty circles to highlight the fact that they are not part of the original sample from M22; the labels used for training and testing are the ones for their corresponding images at  $\mu=28$  mag arcsec $^{-2}$ .

O.K.L.) provided a new classification, which revealed that only 1/4 of the galaxies showing tidal features according to the filtering algorithm were classified as such by all visual classifiers. We believe that the combination of noisy labels, small positive training sample and low surface brightness features to be detected limited the performance of the algorithm. This was the main reason why we decided to use the HSC-like mock images for training the CNN. We note that the original classification by Kado-Fong et al. (2018) used both the images and the output of the filtering algorithm in order to detect features close to the host galaxy, so it is expected that the re-classification of the images alone would yield a lower tidal feature detection rate. On the other hand, as the original Kado-Fong et al. (2018) sample focused on the comparison of the properties of stream and shell hosts, the visual inspection was performed only for the images where a tidal detection was identified by their filtering algorithm, meaning that the completeness of the sample is uncertain.

It is well known that deep learning models are sensitive to the characteristics of the training sample and that thus techniques such as transfer learning (e.g., Domínguez Sánchez et al. 2019) should be used for optimizing models trained on different datasets than the target sample. We attempted, without success, to use transfer learning to fine tune the models on real HSC-data, making exhaustive tests on the number of layers to be trained, the learning rate, etc. The best result we obtained is AUC=0.64, and the output values are concentrated towards the lower end ( $P_{Tidal} < 0.7$ ). These poor results emphasize the strong dependence of the model performance on the data they are trained with and warns us against carelessly applying models to different data domains. It also suggest that mock images from simulations are not as realistic as we might have expected.

A possible explanation for the bad performance could be the differences in the way the mock images were created compared to real HSC data. For example, the angular resolution of the HSC-mock images is poorer (1" vs 0."167 for real HSC-SSP). In addition, the simulated images do not include real backgrounds, processing artifacts, contaminating sources, or sky subtraction residuals. This may compromise the model’s ability to assess real data, as already discussed in Bottrell et al. (2019a). The morphological classification of

TNG simulated images presented in Huertas-Company et al. (2019) was significantly improved by adding realism to the simulated images. Unfortunately, adding realism to the images could change the visual classification used as ‘ground truth’: some features could become undetectable in the presence of brighter objects. Therefore, training the CNN with more realistic mock images and new labels is beyond the scope of the current analysis. We will investigate these possible improvements in the forthcoming studies.

The reason why transfer learning might not solve the domain shift could be the fact that the  $\mu_{lim}$  in the simulated images is not fixed. This implies that the model needs to transfer from many sparsely sampled domains to another, instead of transferring from one well-sampled domain to another. Intuitively, the former may be harder. Another aspect which could have a significant effect is the small parent sample of galaxies used to produce the simulations, based on 36 galaxies only that may not represent the diversity of real galaxy populations. Since the observed sample is flux limited and the simulated sample is volume limited, the former should have a flatter mass distribution with more massive galaxies. Also, the real data have continuous redshift distribution, while the mock images are simulated in five redshift bins. All these differences combine together and it is not possible to investigate each aspect separately with the current sample. Thus, we cannot pinpoint the property that is the main cause of the poor model performance across domains.

## 6 SUMMARY AND CONCLUSIVE REMARKS

Tidal interactions are expected to play a critical role in galaxy mass assembly and evolution, but their low surface brightness make these features difficult to detect. Automated methods for the identification and classifications of tidal features will be compulsory for the analysis of large upcoming surveys such as LSST or Euclid.

In this work, we take advantage of the catalogue presented in M22, that provides tidal feature classifications by professional astronomers for a sample of ~6000 galaxy images from the NEWHORIZON simulations. This constitutes the largest catalogue of visual identifications of tidal features up to date. The galaxies are simulated at different evolutionary times and redshifts and HSC-like mock images with different surface brightness limits ( $\mu_{lim}=28-35$  mag arcsec $^{-2}$ ) were visually inspected by a varying number of professional astronomers (ranging from 2 to 6).

We use a CNN to train a supervised deep learning binary model which aims to reproduce human visual identification of galaxies with tidal features. For this, we have labelled as positives all the images for which a tidal feature was identified by all the classifiers, regardless of the tidal feature category ( $F_{tidal} > 1$ , as detailed in Section 3.2) and as negative those with no tidal identification ( $F_{tidal} = 0$ ). We do not use galaxies for which the presence of a tidal feature was uncertain (disagreement between classifiers). In addition to the original sample, we have created shallower images, more similar to current available observations, at  $\mu_{lim}=26, 27$  mag arcsec $^{-2}$ . These images were not classified in M22 and we use their corresponding labels at  $\mu_{lim}=28$  mag arcsec $^{-2}$  as ground truth. We remark the fact that, since the visual classifications are used as input label to the model, any bias present in human classification would be passed on to the deep learning algorithm (see, for example, how the fraction of tidal detections depends on the image properties in Figure 2). Our main conclusions are:

- The deep learning model is successful in reproducing the human identification of images with tidal features in the HSC-mock images, reaching accuracy, precision and recall values of Acc=0.84, P=0.72

and  $R=0.85$  for the original test sample, using the optimal threshold,  $P_{th}=0.31$ , to select positive cases of tidals.

- The results are surprisingly similar in terms of global accuracy and purity ( $Acc=0.85$ ,  $P=0.71$ ) when the shallower test sample is included, even though these numbers are computed corresponding to the labeling of images one or two orders of magnitude deeper.
- The completeness of the model for the *original+shallow* test sample is smaller than for the *original* one ( $R=0.75$  vs  $R=0.85$ ). There is indeed a clear dependence of the ability of the model to recover tidal features with respect to the image depth: while for  $\mu_{lim} > 30$  mag arcsec<sup>-2</sup> around 90% of the tidal features are recovered, this quantity drops below 50% for  $\mu_{lim} < 28$  mag arcsec<sup>-2</sup> (see Figures 9, 10).
- The accuracy and purity are roughly constant at all surface brightness, hence we conclude that the model is not learning the signal-to-noise of the images, although it is evident that it impacts the classification performance, mostly in terms of completeness, as expected.
- The trend with redshift is not so evident, with the larger AUC values obtained at redshift bins  $z=0.05$  and  $z=0.4$ . The decrease of the fraction of visually identified tidal features at higher redshifts may explain this non-intuitive result (the model is able to correctly recover the true negatives).
- Tidal *streams* and *shells* are the categories easier to identify by the model, with  $TPR=1$  and  $TPR=0.87$ , respectively. On the other hand, *mergers* and *tails* reach only  $TPR=0.68$ ,  $0.69$ , respectively.
- When applied to real HSC images with  $\mu_{lim}=26$  mag arcsec<sup>-2</sup>, the performance is significantly worse than on the simulated images ( $AUC=0.69$ ), even when transfer learning is applied. This is probably related to the fact that the simulated images are not extremely realistic: they have lower spatial resolution than real images and do not include background effects. Besides, they span over a wide  $\mu_{lim}$  range, do not have a uniform redshift coverage and may not include examples of all observed morphological types and/or features.

The results presented in this work represent an important step in the development of automated tidal feature detection techniques, even if the performance is lower than those found in other astronomical classification tasks like separating elliptical from disk galaxies (reaching accuracy above 97%). Tidal feature detection is a difficult task, given the low surface brightness of the subtle structures that we wish to detect. An additional limitation is the lack of a large, homogeneously observed training sample with certain classifications.

One alternative would be to use ‘intrinsic’ labels from simulations, derived from dynamics or merger trees. The disadvantage of such labeling is that observational limitations may not always support the classification of an image in accordance with its intrinsic class. In this work, the training data is assembled from human labels. Labelling tidal features via visual inspection is not trivial and the image pre-processing has a significant impact. In addition, classifiers tend to disagree with each other quite often, as shown in M22. Biases in the identification of interacting galaxies by visual classifications have also been reported in Blumenthal et al. (2020). Therefore, it may not even be possible to achieve an accuracy similar to elliptical/spiral separation due to the much greater ambiguity of the classifications.

We are aware of some important efforts of the scientific community towards building large and robust samples of tidal identifications, such as the detailed annotations presented in Sola et al. (2022); Bilek et al. (2020) or the on-going tidal stream survey by Martínez-Delgado et al. (2021), which will certainly help to construct a robust

training sample to improve the algorithms for automated detection. Approaches such as domain adaptation (Ćiprijanović et al. 2022), the use of unsupervised learning (e.g., Sarmiento et al. 2021; Cheng et al. 2021) or one-shot learning (Chen et al. 2019) could help to overcome the lack of positive training samples currently available, but we leave these approaches for the forthcoming analysis.

The poorer performance of our tidal identification model in the real HSC-SSP images emphasizes the large dependence of deep learning algorithms on the data they are trained with. As already noted in Bottrell et al. (2019a); Huertas-Company et al. (2019); Ćiprijanović et al. (2022), the importance of using realistic simulations for training the models, including background, real noise and artifacts, is fundamental to achieving robust results with real data. This should be taken as a warning against applying deep learning models to different data domains without previously assessing their performance on the new domain.

Our results also highlight the need for deep surveys in order to construct complete samples of galaxies showing tidal interactions. Our predictions imply that we need images with  $\mu_{lim} > 30$  mag arcsec<sup>-2</sup> to achieve completeness above 60%, although given the non-representative sample used for the statistical analysis presented in this work our current result is only suggestive of this requirement. For example, as already noted in Bottrell et al. (2019a) and Bickley et al. (2021), for rare objects amongst large datasets (such as the upcoming LSST) the precision, largely dependent on the assumed fraction of positive instances, is paramount. One could increase the completeness by using larger value of  $P_{th}$ , even if that would decrease the purity, and complement it with visual inspection of a much smaller sample of galaxies.

The challenges facing the automated detection of tidal features should not prevent us from that endeavour. The scientific return of large samples of galaxies showing tidal features is huge. The detection and characterization of these faint tidal remnants – including measurements of their abundance, width, and shapes/morphology – probe the recent merger activity, disruption mechanisms and galaxy mass assembly. Furthermore, the characteristics of observed tidal features can constrain the global properties of the stellar and dark matter haloes (Johnston et al. 1999; Sanderson et al. 2015; Bovy et al. 2016; Pearson et al. 2022) and, consequently, are a complementary way to testing cosmological and dark matter theories. These are, indeed, some of the scientific objectives of the recently approved F-ESA mission ARRAKIHS<sup>5</sup> (P.I. R Guzmán), that will image 50 deg<sup>2</sup> of the sky per year down to an unprecedented ultra-low surface brightness in visible infrared bands (31 and 30 mag arcsec<sup>-2</sup>, respectively). The future of scientific analysis based on tidal features is bright and promising and this work undoubtedly represents an important step forward towards understanding the requirements of an optimal automated identification of such powerful ingredient for galaxy evolution and cosmological studies.

## ACKNOWLEDGEMENTS

We thank the anonymous referee for their suggestions, which helped to improve the clarity of the paper. HDS acknowledges support by the PID2020-115098RJ-I00 grant from

<sup>5</sup> <https://www.cosmos.esa.int/documents/7423467/7423486/ESA-F2-ARRAKIHS-Phase-2-PUBLIC-v0.9.2.pdf/61b363d7-2a06-1196-5c40-c85aa90c2113?t=1667557422996>

MCIN/AEI/10.13039/501100011033 and from the Spanish Ministry of Science and Innovation and the European Union - NextGenerationEU through the Recovery and Resilience Facility project ICTS-MRR-2021-03-CEFCA and AdP and JAO for technical and emotional support. I.D. acknowledges the support of the Canada Research Chair Program and the Natural Sciences and Engineering Research Council of Canada (NSERC, funding reference number RGPIN-2018-05425). FB acknowledges support from the grants PID2020-116188GA-I00 and PID2019-107427GB-C32 by the Spanish Ministry of Science and Innovation. J.H.K. acknowledges financial support from the State Research Agency (AEI-MCINN) of the Spanish Ministry of Science and Innovation under the grant "The structure and evolution of galaxies and their central regions" with reference PID2019-105602GB-I00/10.13039/501100011033, from the ACIISI, Consejería de Economía, Conocimiento y Empleo del Gobierno de Canarias and the European Regional Development Fund (ERDF) under grant with reference PROID2021010044, and from IAC project P/300724, financed by the Ministry of Science and Innovation, through the State Budget and by the Canary Islands Department of Economy, Knowledge and Employment, through the Regional Budget of the Autonomous Community. The authors gratefully acknowledge the computer resources at Artemisa, funded by the European Union ERDF and Comunitat Valenciana as well as the technical support provided by the Instituto de Física Corpuscular, IFIC (CSIC-UV).

## DATA AVAILABILITY

The catalogue used in this article comes from the analysis of M22. The code used for the deep learning algorithm will be shared upon request.

## REFERENCES

- Aihara H., et al., 2018a, *PASJ*, **70**, S4  
 Aihara H., et al., 2018b, *PASJ*, **70**, S8  
 Bickley R. W., et al., 2021, *MNRAS*, **504**, 372  
 Bílek M., et al., 2020, *MNRAS*, **498**, 2138  
 Blumenthal K. A., et al., 2020, *MNRAS*, **492**, 2075  
 Bottrell C., Simard L., Mendel J. T., Ellison S. L., 2019a, *MNRAS*, **486**, 390  
 Bottrell C., et al., 2019b, *MNRAS*, **490**, 5390  
 Bovy J., Bahmanyar A., Fritz T. K., Kallivayalil N., 2016, *ApJ*, **833**, 31  
 Bruzual G., Charlot S., 2003, *MNRAS*, **344**, 1000  
 Bullock J. S., Johnston K. V., 2005, *ApJ*, **635**, 931  
 Chen Z., Fu Y., Zhang Y., Jiang Y.-G., Xue X., Sigal L., 2019, *IEEE Transactions on Image Processing*, **28**, 4594  
 Cheng T.-Y., et al., 2020, *MNRAS*, **493**, 4209  
 Cheng T.-Y., Huertas-Company M., Conselice C. J., Aragón-Salamanca A., Robertson B. E., Ramachandra N., 2021, *MNRAS*, **503**, 4446  
 Ćiprijanović A., et al., 2022, *Machine Learning: Science and Technology*, **3**, 035007  
 Cole S., Lacey C. G., Baugh C. M., Frenk C. S., 2000, *MNRAS*, **319**, 168  
 Conselice C. J., Bershady M. A., Jangren A., 2000, *ApJ*, **529**, 886  
 Conselice C. J., Mundy C. J., Ferreira L., Duncan K., 2022, arXiv e-prints, p. arXiv:2207.03984  
 Cooper A. P., D'Souza R., Kauffmann G., Wang J., Boylan-Kolchin M., Guo Q., Frenk C. S., White S. D. M., 2013, *MNRAS*, **434**, 3348  
 Dieleman S., Willett K. W., Dambre J., 2015, *MNRAS*, **450**, 1441  
 Domínguez Sánchez H., Huertas-Company M., Bernardi M., Tuccillo D., Fischer J. L., 2018, *MNRAS*, **476**, 3661  
 Domínguez Sánchez H., et al., 2019, *MNRAS*, **484**, 93  
 Domínguez Sánchez H., Margalef B., Bernardi M., Huertas-Company M., 2022, *MNRAS*, **509**, 4024  
 Draine B. T., et al., 2007, *ApJ*, **663**, 866  
 Dubois Y., et al., 2014, *MNRAS*, **444**, 1453  
 Dubois Y., et al., 2021, *A&A*, **651**, A109  
 Duc P.-A., et al., 2015, *MNRAS*, **446**, 120  
 Fall S. M., Efstathiou G., 1980, *MNRAS*, **193**, 189  
 Fitts A., et al., 2018, *MNRAS*, **479**, 319  
 Ghosh A., Urry C. M., Wang Z., Schawinski K., Turp D., Powell M. C., 2020, *ApJ*, **895**, 112  
 Gwyn S. D. J., 2012, *AJ*, **143**, 38  
 Hausen R., Robertson B. E., 2020, *ApJS*, **248**, 20  
 He K., Zhang X., Ren S., Sun J., 2016, in 2016 IEEE Conference on Computer Vision and Pattern Recognition (CVPR). pp 770–778, doi:10.1109/CVPR.2016.90  
 Helmi A., White S. D. M., 1999, *MNRAS*, **307**, 495  
 Hendel D., Johnston K. V., 2015, *MNRAS*, **454**, 2472  
 Hernquist L., Quinn P. J., 1989, *ApJ*, **342**, 1  
 Hood C. E., Kannappan S. J., Stark D. V., Dell'Antonio I. P., Moffett A. J., Eckert K. D., Norris M. A., Hendel D., 2018, *ApJ*, **857**, 144  
 Huang Q., Fan L., 2022, *ApJS*, **262**, 39  
 Huertas-Company M., Lanusse F., 2022, arXiv e-prints, p. arXiv:2210.01813  
 Huertas-Company M., et al., 2015, *ApJS*, **221**, 8  
 Huertas-Company M., et al., 2019, *MNRAS*, **489**, 1859  
 Huško F., Lacey C. G., Baugh C. M., 2022, arXiv e-prints, p. arXiv:2207.07139  
 Iodice E., et al., 2017, *ApJ*, **839**, 21  
 Ivezić Ž., et al., 2019, *ApJ*, **873**, 111  
 Javanmardi B., et al., 2016, *A&A*, **588**, A89  
 Ji L., Peirani S., Yi S. K., 2014, *A&A*, **566**, A97  
 Johnston K. V., Majewski S. R., Siegel M. H., Reid I. N., Kunkel W. E., 1999, *AJ*, **118**, 1719  
 Johnston K. V., Bullock J. S., Sharma S., Font A., Robertson B. E., Leitner S. N., 2008, *ApJ*, **689**, 936  
 Kado-Fong E., et al., 2018, *ApJ*, **866**, 103  
 Komatsu E., et al., 2011, *ApJS*, **192**, 18  
 Lacey C., Cole S., 1993, *MNRAS*, **262**, 627  
 Lanusse F., Ma Q., Li N., Collett T. E., Li C.-L., Ravanbakhsh S., Mandelbaum R., Póczos B., 2018, *MNRAS*, **473**, 3895  
 Laureijs R., et al., 2011, arXiv e-prints, p. arXiv:1110.3193  
 Lofthouse E. K., Kaviraj S., Conselice C. J., Mortlock A., Hartley W., 2017, *MNRAS*, **465**, 2895  
 López-Sanjuan C., et al., 2012, *A&A*, **548**, A7  
 Lotz J. M., Jonsson P., Cox T. J., Croton D., Primack J. R., Somerville R. S., Stewart K., 2011, *ApJ*, **742**, 103  
 Lupton R., Blanton M. R., Fekete G., Hogg D. W., O'Mullane W., Szalay A., Wherry N., 2004, *PASP*, **116**, 133  
 Mancillas B., Duc P.-A., Combes F., Bournaud F., Emsellem E., Martig M., Michel-Dansac L., 2019, *A&A*, **632**, A122  
 Martin G., Kaviraj S., Devriendt J. E. G., Dubois Y., Laigle C., Pichon C., 2017, *MNRAS*, **472**, L50  
 Martin G., Kaviraj S., Devriendt J. E. G., Dubois Y., Pichon C., 2018, *MNRAS*, **480**, 2266  
 Martin G., et al., 2021, *MNRAS*, **500**, 4937  
 Martin G., et al., 2022, *MNRAS*, **513**, 1459  
 Martínez-Delgado D., Pohlen M., Gabany R. J., Majewski S. R., Peñarrubia J., Palma C., 2009, *ApJ*, **692**, 955  
 Martínez-Delgado D., et al., 2010, *AJ*, **140**, 962  
 Martínez-Delgado D., et al., 2021, arXiv e-prints, p. arXiv:2104.06071  
 Mihos J. C., Dubinski J., Hernquist L., 1998, *ApJ*, **494**, 183  
 Mihos J. C., Harding P., Feldmeier J. J., Rudick C., Janowiecki S., Morrison H., Slater C., Watkins A., 2017, *ApJ*, **834**, 16  
 Miyazaki S., et al., 2012, in McLean I. S., Ramsay S. K., Takami H., eds, Society of Photo-Optical Instrumentation Engineers (SPIE) Conference Series Vol. 8446, Ground-based and Airborne Instrumentation for Astronomy IV. p. 84460Z, doi:10.1117/12.926844



- Montes M., Infante-Sainz R., Madrigal-Aguado A., Román J., Monelli M., Borlaff A. S., Trujillo I., 2020, *ApJ*, **904**, 114
- Montes M., Brough S., Owers M. S., Santucci G., 2021, *ApJ*, **910**, 45
- Morales G., Martínez-Delgado D., Grebel E. K., Cooper A. P., Javanmardi B., Miskolczi A., 2018, *A&A*, **614**, A143
- O’Leary J. A., Moster B. P., Naab T., Somerville R. S., 2021, *MNRAS*, **501**, 3215
- Pearson S., Price-Whelan A. M., Hogg D. W., Seth A. C., Sand D. J., Hunt J. A. S., Crnojević D., 2022, *ApJ*, **941**, 19
- Pillepich A., et al., 2014, *MNRAS*, **444**, 237
- Qu Y., et al., 2017, *MNRAS*, **464**, 1659
- Robertson B., Bullock J. S., Cox T. J., Di Matteo T., Hernquist L., Springel V., Yoshida N., 2006, *ApJ*, **645**, 986
- Rodríguez-Gomez V., et al., 2016, *MNRAS*, **458**, 2371
- Rodríguez-Puebla A., Primack J. R., Avila-Reese V., Faber S. M., 2017, *MNRAS*, **470**, 651
- Salpeter E. E., 1955, *ApJ*, **121**, 161
- Sanderson R. E., Helmi A., Hogg D. W., 2015, *ApJ*, **801**, 98
- Sarmiento R., Huertas-Company M., Knapen J. H., Sánchez S. F., Domínguez Sánchez H., Drory N., Falcón-Barroso J., 2021, *ApJ*, **921**, 177
- Sola E., et al., 2022, *A&A*, **662**, A124
- Spavone M., et al., 2018, *ApJ*, **864**, 149
- Spavone M., et al., 2020, *A&A*, **639**, A14
- Tan M., Le Q. V., 2019, arXiv e-prints, p. [arXiv:1905.11946](https://arxiv.org/abs/1905.11946)
- Thorp M. D., Bluck A. F. L., Ellison S. L., Maiolino R., Conselice C. J., Hani M. H., Bottrell C., 2021, *MNRAS*, **507**, 886
- Valenzuela L. M., Remus R.-S., 2022, arXiv e-prints, p. [arXiv:2208.08443](https://arxiv.org/abs/2208.08443)
- Vega-Ferrero J., et al., 2021, *MNRAS*, **506**, 1927
- Vera-Casanova A., et al., 2022, *MNRAS*, **514**, 4898
- Walmsley M., Ferguson A. M. N., Mann R. G., Lintott C. J., 2019, *MNRAS*, **483**, 2968
- Walmsley M., et al., 2022, *MNRAS*, **509**, 3966
- Weingartner J. C., Draine B. T., 2001, *ApJ*, **548**, 296
- White S. D. M., Frenk C. S., 1991, *ApJ*, **379**, 52
- White S. D. M., Rees M. J., 1978, *MNRAS*, **183**, 341
- van Dokkum P. G., et al., 2010, *ApJ*, **709**, 1018

This paper has been typeset from a  $\text{\TeX}/\text{\LaTeX}$  file prepared by the author.